PHILOSOPHICAL TRANSACTIONS A

royalsocietypublishing.org/journal/rsta

Research

Cite this article: Jaworski JW. 2019 Sound from aeroelastic vortex–fibre interactions. *Phil. Trans. R. Soc. A* **377**: 20190071. http://dx.doi.org/10.1098/rsta.2019.0071

Accepted: 12 September 2019

One contribution of 12 to a theme issue 'Frontiers of aeroacoustics research: theory, computation and experiment'.

Subject Areas:
applied mathematics, acoustics, fluid mechanics

Keywords:
conformal mapping, vortex sound, point vortex dynamics, fluid–structure interactions, silent owl flight

Author for correspondence:
J. W. Jaworski
e-mail: jaworski@lehigh.edu

THE ROYAL SOCIETY PUBLISHING

Sound from aeroelastic vortex–fibre interactions

J. W. Jaworski

Department of Mechanical Engineering and Mechanics, Lehigh University, Bethlehem, PA, USA

JWJ, 0000-0002-0746-7661

The motion of a line vortex moving past a one-dimensional flexible fibre is examined theoretically. A Schwarz–Christoffel conformal mapping enables the analytical solution of the potential flow field and its hydrodynamic moment on the flexible fibre, which is composed of a rigid segment constrained to angular motions on a wedge. The hydroelastic coupling of the vortex path and fibre motion affects the noise signature, which is evaluated for the special case of acoustically compact fibres embedded in a half plane. Results from this analysis attempt to address how the coupled interactions between vortical sources and flexible barbules on the upper surface of owl wings may contribute to their acoustic stealth. The analytical formulation is also amenable to application to vortex sound prediction from flexible trailing edges provided that an appropriate acoustic Green's function can be determined.

This article is part of the theme issue 'Frontiers of aeroacoustics research: theory, computation and experiment'.

1. Introduction

Owls are believed to fly in effective silence as a result of three distinctive and unique physical features [1]: a comb of stiff feathers at the wing leading edge, a fringe of flexible filaments at the trailing edges of the feathers and wing, and a soft downy coating on the upper wing surface. In contrast to the amount of research literature devoted to leading- and trailing-edge modifications for turbulence noise mitigation [2–13], the mechanisms for acoustic attenuation by the downy material on owl wings have received relatively little attention. Despite this lack of research activity, Lilley [14] postulated that the down material was essential to the owl 'hush kit', suggesting that the large bandwidth of noise suppression resulted from a mechanism of the

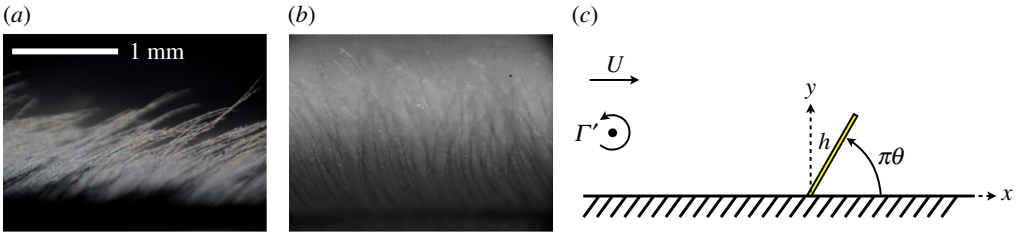

Figure 1. Representation of owl down barbules (great grey owl, *Strix nebulosa*, (*a*); snowy owl, *Nyctea scandiaca*, (*b*)) on the upper surface of flight feathers as a two-dimensional fibre (*c*) that is elastically restrained to rotate about the origin. A point vortex of strength Γ' represents a turbulent eddy immersed in a uniform fluid flow with speed U. (Online version in colour.)

down to eliminate turbulence noise at its source. Clark *et al*. [15] discovered the unique structure of the down material, which is composed of several flexible barbules (fibres) that interlock to form a porous barrier that offsets the boundary-layer flow and its noise sources from the wing surface by a distance of the order of a millimetre. Their experiments with various porous canopies demonstrated that surface pressure fluctuation level reductions of up to 30 dB could be achieved with this small offset, and complementary theoretical models developed in that investigation linked the low-frequency level reductions to the mixing-layer instability occurring at the suspended porous layer. This work led to the development of rigid, streamwise-aligned structures termed 'finlets' designed to modify the boundary layer upstream of the trailing edge before encountering the trailing edge, which yielded frequency-dependent far-field noise reductions of up to 10 dB on a DU96-W180 aerofoil section relative to its untreated counterpart [16]. Jaworski & Peake [17] provide a detailed review of this and other noise-reduction technologies inspired by the aeroacoustics of owls.

The present study extends the theoretical model of Clark *et al*. [15] to include the effect of *hydroelastic fibre motions* on the motion of the incoming vortex and the resulting noise generation. A single fibre is modelled to represent the physical limit of a sparse distribution of down fibres, as illustrated in figure 1. The basic idea here is to determine what role the hydrodynamic movement of the flexible down fibres in the presence of an advecting vortex has on the strength of its acoustic field relative to its stationary-fibre counterpart. Previous works have addressed the vortex noise generation from rigid fibres perpendicular to a half-plane [18–20], and the Schwarz–Christoffel conformal mapping of Clark *et al*. [15] and Lighthill [21] for arbitrary fibre inclinations enable the analysis of coupled dynamic motions of the vortex and fibre. A generalized mathematical model for a vortex moving past a rigid wedge with a movable fibre extending from its vertex is presented in §2, which includes the special case of a flexible fibre extending from a half plane investigated in this paper. A theoretical framework for the hydrodynamic coupling between the rotational motion of the fibre to the vortex path is also presented. Section 3 investigates the dynamic aeroelastic coupling between the angular motions of the elastically restrained fibre and the vortex path in a steady mean flow, and the resulting noise generation is estimated from vortex sound theory [20]. Conclusions from this investigation are presented in §4.

2. Mathematical model

(a) Conformal mapping

The mathematical analysis for sound due to a vortex passing round an inclined fibre (cf. figure 2) follows from the procedure outlined by Howe [20] for a vortex passing over a rigid, upright spoiler in a background mean flow, which was extended for arbitrary angles of inclination $\theta \in (0, 1)$ by Clark *et al*. [15] and whose surface geometry appears in Lighthill [21] in the context of the Weis-Fogh clap-and-fling lift mechanism. The present paper generalizes the half plane in these

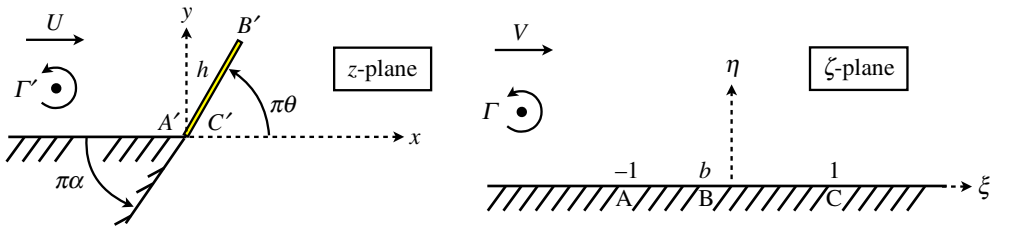

Figure 2. Generalized conformal mapping of a wedge with a finite extension from its tip. The Schwarz–Christoffel transformation relates the physical z-plane to the ζ-plane where the vortex motion problem is solved. The impermeable wall condition is satisfied automatically by adding an appropriate image vortex in the solid boundary that is complemented by a kinematic boundary condition on the fibre. For conformal maps, $\Gamma' = \Gamma$. Uniform background flows are considered only when $\alpha = 1$ for the case of a half plane. (Online version in colour.)

works to an arbitrary wedge, which may also be used for vortex sound analyses of trailing edges. The mapping between the physical z-plane and the ζ-plane is achieved using the Schwarz–Christoffel transformation [22]

$$z = \frac{K}{2-\alpha}(\zeta+1)^{1-\theta}(\zeta-1)^{1-\alpha+\theta}. \tag{2.1}$$

The mapping constants b and K are determined by linking the z- and ζ-planes, yielding

$$b = \frac{\alpha-2\theta}{2-\alpha} \quad \text{and} \quad K = \frac{(2-\alpha)h}{f(\alpha,\theta)}, \tag{2.2}$$

where

$$f(\alpha,\theta) = \frac{2^{2-\alpha}(1-\theta)^{1-\theta}(1-\alpha+\theta)^{1-\alpha+\theta}}{(2-\alpha)^{2-\alpha}} \mathrm{e}^{\mathrm{i}\pi(1-\alpha)}. \tag{2.3}$$

The expression $f(\alpha,\theta) = \exp(\mathrm{i}\pi(1-\alpha))g(\alpha,\theta)$ defines real-valued $g(\alpha,\theta)$. The mapping between the z- and ζ-planes is completed by equating the background mean flows far from the fibre, which can be achieved for finite flow speeds only in the special case of the planar wall ($\alpha = 1$) [23, (pp. 410–412)], where $V = KU$.

(b) Equations of vortex motion

The nonlinear equations for the motion of the vortex at $z_0(t) = x_0(t) + \mathrm{i}\, y_0(t)$ are

$$\begin{aligned}\frac{\mathrm{d}\bar{z}_0}{\mathrm{d}t} &= \frac{\mathrm{d}x_0}{\mathrm{d}t} - \mathrm{i}\frac{\mathrm{d}y_0}{\mathrm{d}t} \\ &= -\frac{\mathrm{i}\Gamma}{4\pi}\frac{\zeta''(z_0)}{\zeta'(z_0)} + \left(\frac{\mathrm{i}\Gamma}{2\pi}\frac{1}{\zeta(z_0)-\bar{\zeta}(z_0)} + UK - \frac{h^2}{4}\frac{\mathrm{d}\theta}{\mathrm{d}t}\int_{-1}^{1}\frac{|Z_\mathrm{f}(\chi,\alpha,\theta)|^2}{(\chi-\zeta(z_0))^2}\,\mathrm{d}\chi\right)\zeta'(z_0),\end{aligned} \tag{2.4}$$

where

$$\frac{\zeta''(z_0)}{\zeta'(z_0)} = \left[\theta(\zeta+1)^{-1} - (\zeta-b)^{-1} + (\alpha-\theta)(\zeta-1)^{-1}\right]\zeta'(z_0). \tag{2.5}$$

Here the primes denote $(\,)' = \mathrm{d}/\mathrm{d}z$, and the integral

$$I(\zeta,\alpha,\theta) = \int_{-1}^{1}\frac{|Z_\mathrm{f}(\chi,\alpha,\theta)|^2}{(\chi-\zeta)^2}\,\mathrm{d}\chi \tag{2.6}$$

follows from the kinematic boundary condition imposed on the moving fibre, which is detailed in appendix A; equation (A 7) defines function $|Z_\mathrm{f}|$. In general, (2.4) depends implicitly on the vortex

position through $\zeta(z_0)$, which requires the solution of (2.1) for a given z_0. The vortex equations of motion (2.4) can be expressed in dimensionless form

$$\frac{\mathrm{d}\bar{Z}}{\mathrm{d}T} = \left\{-\mathrm{i}\frac{f(\alpha,\theta)}{2-\alpha}\left[\theta(\zeta+1)^{-1} - (\zeta-b)^{-1} + (\alpha-\theta)(\zeta-1)^{-1} - \frac{2}{\zeta-\bar{\zeta}} - \mathrm{i}\frac{1}{4}\frac{\mathrm{d}\theta}{\mathrm{d}T}I(\zeta,\alpha,\theta)\right] + \epsilon\right\} \times (\zeta+1)^{\theta}(\zeta-b)^{-1}(\zeta-1)^{\alpha-\theta}, \tag{2.7}$$

where $\zeta = \zeta(Z)$, using the following dimensionless groups:

$$Z = \frac{z_0}{h}, \quad S = \frac{\Gamma}{4\pi h}, \quad T = \frac{tS}{h}, \quad \epsilon = \frac{U}{S}. \tag{2.8}$$

(c) Dynamic fibre model

The vortex equations of motion (2.7) hold generally for all fibre angles, which in the dynamic case $\theta = \theta(t)$. The fibre motion may be either prescribed or be the solution of an oscillator model for the perturbation angle $\hat{\theta}$ about elastic equilibrium position θ_0, such that $\theta = \theta_0 + \hat{\theta}$. The linear oscillator model considered here is

$$I_0\frac{\mathrm{d}^2\hat{\theta}}{\mathrm{d}t^2} + c_\theta\frac{\mathrm{d}\hat{\theta}}{\mathrm{d}t} + k_\theta\hat{\theta} = M_0, \tag{2.9}$$

which in dimensionless form may be written as

$$\frac{\mathrm{d}^2\hat{\theta}}{\mathrm{d}T^2} + 2\Omega c_d\frac{\mathrm{d}\hat{\theta}}{\mathrm{d}T} + \Omega^2\hat{\theta} = \mu^{-1}C_{M_0}. \tag{2.10}$$

Here $\omega_\theta^2 = k_\theta/I_\theta$, $\Omega = \omega_\theta h/S$, $\mu = I_0/(\rho h^4)$, $c_d = c_\theta/(2I_0\omega_\theta)$, $C_{M_0} = M_0/(\rho S^2h^2)$ and ρ is the fluid density. The coefficient of moment C_{M_0} is computed by integrating the instantaneous pressure difference across the fibre times its moment arm from the elastic axis. Four integral terms arise that represent individual contributions from the unsteady and dynamic head portions of the linearized Bernoulli equation evaluated on the fibre surface. These integrals are first formulated in the z-plane and then recast as integrations along the ξ-axis in the ζ-plane.

The total unsteady moment coefficient in the anti-clockwise direction is

$$C_{M_0} = \frac{2-\alpha}{g^2(\alpha,\theta)}\left[M_1\frac{\mathrm{d}^2\theta}{\mathrm{d}T^2} + M_2\left(\frac{\mathrm{d}\theta}{\mathrm{d}T}\right)^2 + M_3\left|\frac{\mathrm{d}Z}{\mathrm{d}T}\right| + M_4\right]. \tag{2.11}$$

Time-dependent coefficients M_1, M_2 and M_3 are integrals resulting from the unsteady pressure contribution and are given in appendix B. Coefficient M_4 is linked to the moment contribution associated with the dynamic head,

$$M_4 = -\frac{1}{2}\fint_{-1}^{1}\frac{(A^2+\epsilon^2-2A\epsilon\cos\pi\alpha)(1-\xi^2)}{\xi-b}\,\mathrm{d}\xi, \tag{2.12}$$

where the Cauchy principal value must be taken, and

$$A = \frac{g(\alpha,\theta)}{2-\alpha}\left(\frac{4\eta_0(T)}{(\xi-\xi_0(T))^2+\eta_0^2(T)} - \frac{1}{4}\frac{\mathrm{d}\theta}{\mathrm{d}T}I(\xi,\alpha,\theta)\right). \tag{2.13}$$

Moment integrals (2.12) and (B 1)–(B 3) determine the instantaneous hydrodynamic moment (2.11) in (2.10) acting on the flexible fibre, which can be evaluated using standard numerical integration routines. A fully hydroelastic numerical simulation of the vortex–fibre interaction round a generalized wedge is made possible with the present approach by integrating (2.7) and (2.10) forward in time. In addition to the owl down model problem considered in this paper, this numerical framework also enables the examination of vortex sound generation from link models of flexible trailing edges with finite or zero trailing-edge angles for cases where $\alpha < 1$, which is beyond the scope of this paper but will be pursued in future work. In addition, the singular flow velocity at the fibre tip in the present theoretical model may be regularized by vortex shedding,

which could be pursued using point vortices or other low-order models [24–28] to investigate this vorticity production on the acoustic signature.

(d) Acoustic emission

In the special case of a fibre protruding from a half plane ($\alpha = 1$, cf. figure 1), the acoustic emission from the fibre can be expressed in terms of the vortex path, the fibre angular motion and the streamwise component of the Kirchhoff vector, provided that the fibre is acoustically compact. Under this assumption, Howe [20, (p. 193)] defines a function

$$\mathcal{W}(Z) = \frac{\mathrm{d}}{\mathrm{d}z}(K\zeta) = (\zeta+1)^{\theta}(\zeta-b)^{-1}(\zeta-1)^{\alpha-\theta}, \tag{2.14}$$

such that the reduced acoustic pressure in the far field due to the vortex motion is

$$P_{\Gamma}(\mathbf{x},t) \equiv \frac{p_{\Gamma}(\mathbf{x},t)}{\rho S^2\sqrt{M}\sin\beta\,(h/|\mathbf{x}|)^{1/2}} \approx 2^{5/2}\frac{\partial}{\partial T}\int_0^{\infty} \mathrm{Im}\left[\mathcal{W}(Z)\frac{\mathrm{d}Z}{\mathrm{d}\hat{T}}([T]-\lambda^2)\right]\mathrm{d}\lambda. \tag{2.15}$$

The second term of the integrand implies the functional dependence $\mathrm{d}Z/\mathrm{d}\hat{T}([T]-\lambda^2) = u([T]-\lambda^2) + \mathrm{i}v([T]-\lambda^2)$, and $\hat{T} = [T]-\lambda^2$. Equation (2.15) measures the acoustic pressure at far-field location $\mathbf{x}$, which is inclined at an angle β measured clockwise from the y-direction. In (2.15), c_0 is the isentropic speed of sound, the Mach number is defined as $M = S/c_0$, and $[T]$ is the non-dimensional retarded time [15]. It is worthwhile to note that the influence of the fibre position on the vortex sound is handled intrinsically by the time dependence of θ in $\mathcal{W}(Z)$.

The acceleration of the fibre generates an additional dipolar acoustic emission that must also be included in the total acoustic field [26]. The pressure contribution from the fibre acceleration is [20, (p. 127)]

$$p_{\mathrm{f}}(\mathbf{x},t) = \rho\int_{-\infty}^{\infty}\oint_{S_{\mathrm{f}}}\frac{\partial v_{\mathrm{n}}}{\partial\tau}(\mathbf{y},\tau)G(\mathbf{x},\mathbf{y},t-\tau)\,\mathrm{d}S_{\mathrm{f}}(\mathbf{y})\,\mathrm{d}\tau, \quad |\mathbf{x}|\to\infty, \tag{2.16}$$

where v_{n} is the velocity normal to the moving solid boundary S_{f}. The compact Green's function for a compact body at a plane wall is [20, (p. 138)]

$$G(\mathbf{x},\mathbf{y},t-\tau) \approx \frac{x\,Y_1}{\pi\sqrt{2c_0}|\mathbf{x}|^{3/2}}\frac{\partial}{\partial t}\left\{\frac{H(t-\tau-|\mathbf{x}|/c_0)}{\sqrt{t-\tau-|\mathbf{x}|/c_0}}\right\}, \quad |\mathbf{x}|\to\infty, \tag{2.17}$$

which involves Heaviside function H. The term Y_1 denotes the first component of the Kirchhoff vector that corresponds to the ideal flow of unit speed in the x-direction passing round the fibre, which in this configuration is $Y_1 = \mathrm{Re}[K\zeta] = h\xi/g(\alpha=1,\theta)$. Equation (2.16) may be reorganized using (2.1), (2.8) and (2.17) to identify the reduced acoustic pressure from fibre acceleration

$$P_{\mathrm{f}}(\mathbf{x},t) \approx -\frac{2^{1/2}}{\pi}\frac{\partial}{\partial T}\int_0^{\infty}\left[\frac{I_{\mathrm{f}}(\theta)}{g^3(\alpha=1,\theta)}\frac{\mathrm{d}^2\theta}{\mathrm{d}\hat{T}^2}\right]([T]-\lambda^2)\,\mathrm{d}\lambda, \tag{2.18}$$

using the same pressure scaling as in (2.15). The expression in the brackets of (2.18) is a function of $\hat{T} = [T]-\lambda^2$, and

$$I_{\mathrm{f}}(\theta) = \int_{-1}^{1-2\theta}F(\xi,\theta)\,\mathrm{d}\xi - \int_{1-2\theta}^{1}F(\xi,\theta)\,\mathrm{d}\xi, \tag{2.19}$$

where

$$F(\xi,\theta) = \xi[\xi-(1-2\theta)](1+\xi)^{1-2\theta}(1-\xi)^{2\theta-1}. \tag{2.20}$$

The total reduced pressure in the acoustic far field is $P(\mathbf{x},t) = P_{\Gamma}(\mathbf{x},t) + P_{\mathrm{f}}(\mathbf{x},t)$.

3. Results

Previous works have considered the sound generated by a vortex passing over an oscillating [21] or a stationary, upright [18–20] or leaning [15] two-dimensional barrier emerging from a half plane. The mathematical model presented in §2 extends beyond these works in two ways. First,

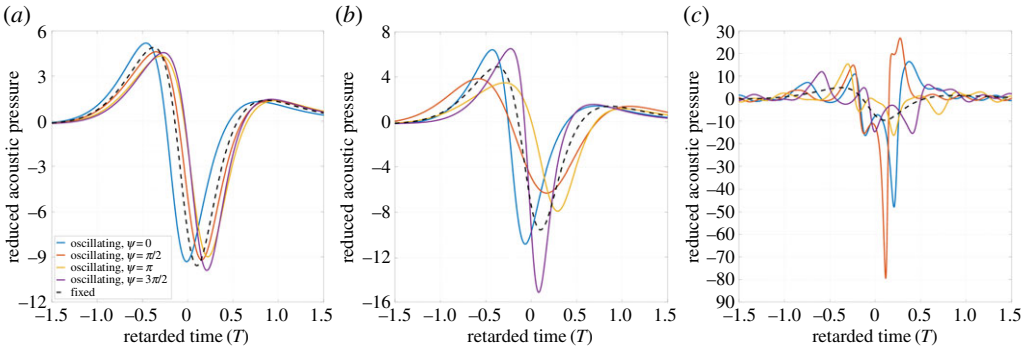

Figure 3. Dependence of the acoustic signature on oscillation frequency of the fibre ω and initial phase ψ relative to the fixed fibre case without a mean flow, $\epsilon = 0$: (*a*) $\omega = 0.1$; (*b*) $\omega = 1$; (*c*) $\omega = 10$. The retarded time [T] is referenced to the instant the vortex passes $x = 0$. (Online version in colour.)

the unsteady fibre motion and resulting hydrodynamic moment due to an incident vortex are modelled. Second, the half plane is generalized as a solid wedge, which enables vortex motion prediction round edges of arbitrary wedge angle with an elastic extension. In this paper, the path of a vortex in a uniform flow and its interaction with prescribed, harmonic fibre motions or aeroelastic motions due to hydrodynamic vortex–fibre coupling are evaluated to anticipate their effect on the far-field acoustic signature.

(a) Prescribed fibre motion

To form a basis for comparison against prior works, all vortex paths investigated herein start far upstream of the fibre at $Z = -10 + 0.75\mathrm{i}$ unless stated otherwise. The fibre angular position is described by $\theta(T) = \theta_0 + \theta_1 \sin(\omega T + \psi)$, where $\theta_0 = 0.5$ and $\theta_1 = 0.1$ to produce a harmonic oscillation about the upright fibre position. The relative starting positions of the vortex and fibre are phased by $\psi = 0, \pi/2, \pi$ and $3\pi/2$, and the frequency is varied across $\omega = 0.1, 1$ and 10. Vortex trajectories and acoustic emissions are investigated for scenarios without ($\epsilon = 0$) and with ($\epsilon > 0$) a background mean flow.

In the absence of a mean flow, figure 3 shows the influence of the fibre oscillation frequency and the initially phasing between the vortex and fibre on the reduced acoustic pressure, as compared to the limiting case of a stationary, upright fibre, whose results have been verified against the literature [19,20]. To facilitate comparison, the retarded time is referenced with respect to when the vortex crosses $x = 0$. For $\omega = 0.1$ and $\omega = 1$, the effect of the change in phase angle ψ is predominantly to shift the acoustic signature left or right, which agrees with the shift in the vortex path in figure 4*a*,*b*. The extrema of the acoustic signals increase with the oscillating frequency ω, with the exception of $\omega = 1$ when $\psi = \pi/2$ or $3\pi/2$. In these cases, figure 4*b* indicates that the phase between the vortex and fibre motion increases the minimum distance between the two, leading to a weaker acoustic emission. For the largest oscillating frequency considered, $\omega = 10$, it is clear that prescribed fibre motion modulates the acoustic signal and leads to large increases in the acoustic noise level. These results are consistent with the fact that a larger relative velocity between the vortex and fibre when in close proximity leads to peaks in the acoustic signature. The high oscillation frequency also affects the vortex trajectory, bringing the vortex nearer the fibre and breaking strongly the left–right symmetry of the vortex path.

The qualitative parametric trends for $\epsilon = 0$ also hold when a mean flow of magnitude $\epsilon = 1$ is introduced in figures 5 and 6. With mean flow, a case is again found for $\omega = 1$ when the oscillating fibre creates a weaker acoustic output than for a fixed fibre, occurring instead at $\psi = 0$, which indicates that the background flow also plays a substantial role in the phasing between the vortex and fibre motions. As anticipated, the acoustic pressure extrema occur at greater magnitudes due to the enhanced relative velocities between the vortex and fibre when in closest proximity.

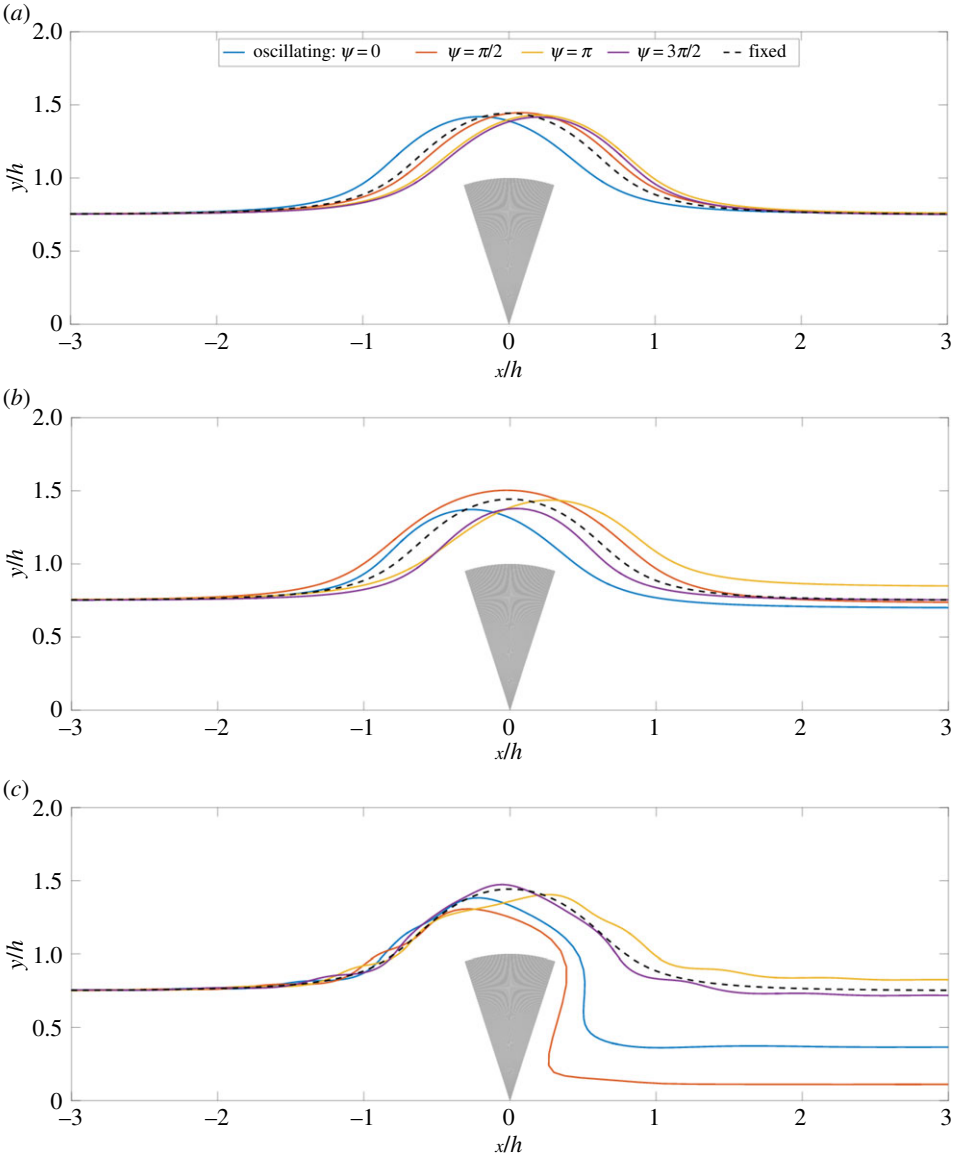

Figure 4. Vortex trajectories past an oscillating fibre of frequency ω with initial phase ψ without a mean flow, $\epsilon = 0$: (*a*) $\omega = 0.1$; (*b*) $\omega = 1$; (*c*) $\omega = 10$. The grey sector indicates the region in which the fibre oscillates. (Online version in colour.)

These results for vortex sound generated by a fibre oscillating with prescribed motion suggest at least two strategies in which fibre unsteadiness could weaken the resulting acoustic emission. First, if the phasing of the motion influences the vortex trajectory in a way that increases the minimum distance between the vortex and fibre, the peaks of the acoustic signature are reduced. Second, the acoustic emission is reduced when the speed of the vortex in close proximity to the fibre is reduced. These strategies based on the dynamic vortex–fibre interplay are supported by the fact that the reduced acoustic pressure P_Γ due to the vortex dominates the total acoustic field. The radiation due to the angular acceleration of the fibre is largest (but still relatively insignificant) for $\omega = 10$ with an amplitude of $|P_{\mathrm{f}}| \approx 1.04$; this acoustic pressure amplitude changes by a factor of ω^2 to render this contribution negligible at smaller fibre vibration frequencies.

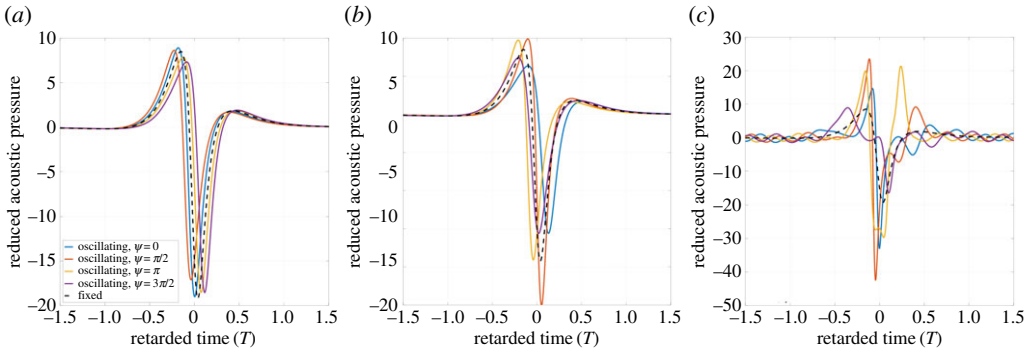

Figure 5. Dependence of the acoustic signature on oscillation frequency of the fibre ω and initial phase ψ relative to the fixed fibre case with a mean flow, $\epsilon = 1$: (*a*) $\omega = 0.1$; (*b*) $\omega = 1$; (*c*) $\omega = 10$. The retarded time [*T*] is referenced to the instant the vortex passes $x = 0$. (Online version in colour.)

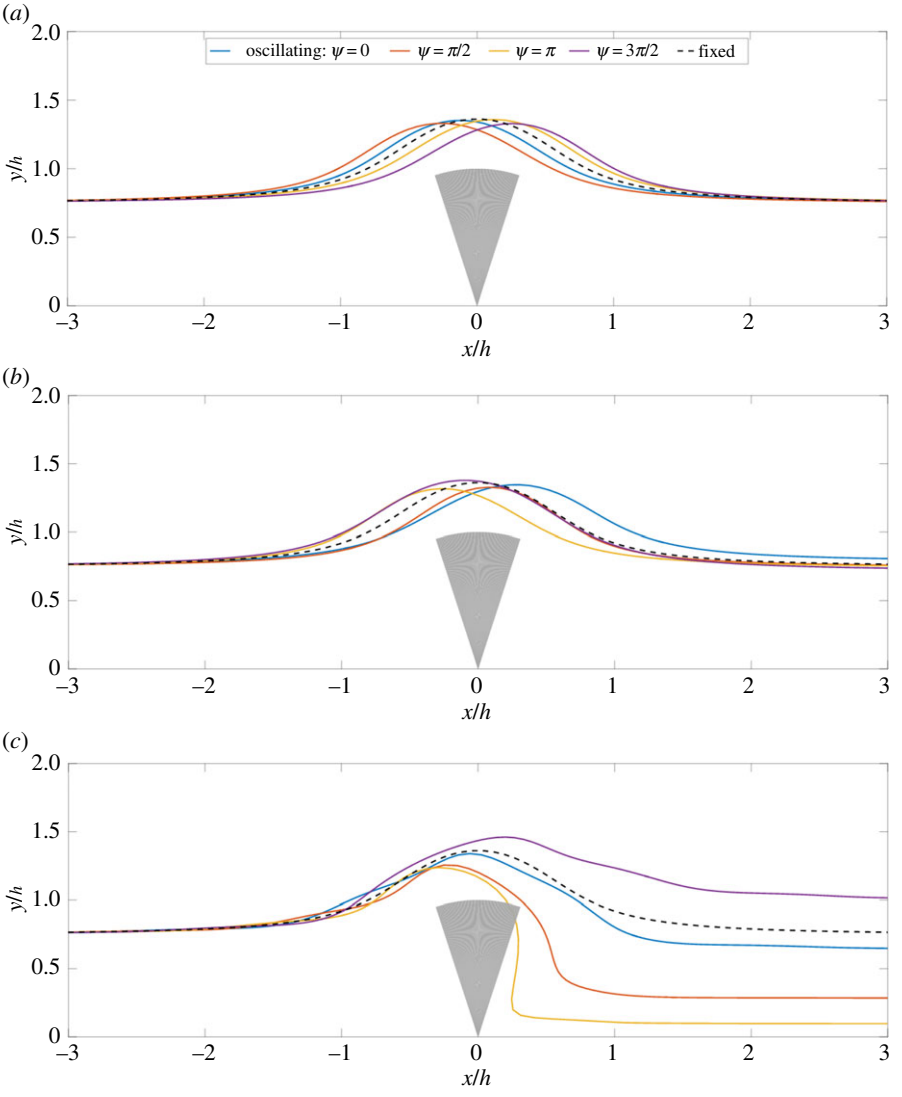

Figure 6. Vortex trajectories past an oscillating fibre of frequency ω with initial phase ψ with mean flow, $\epsilon = 1$: (*a*) $\omega = 0.1$; (*b*) $\omega = 1$; (*c*) $\omega = 10$. The grey sector indicates the region in which the fibre oscillates. (Online version in colour.)

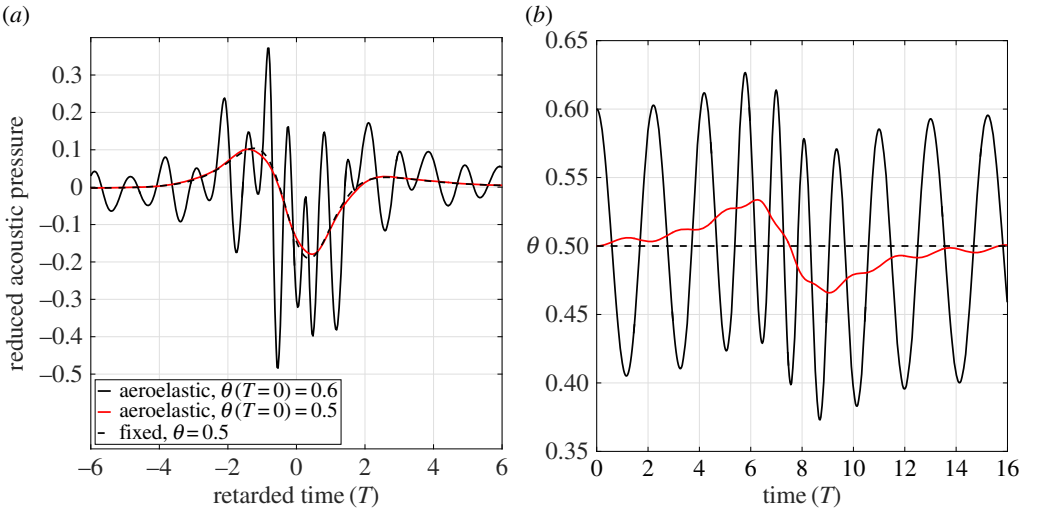

Figure 7. Dynamic and acoustic responses of a flexible fibre immersed in a uniform flow that is aeroelastically coupled to an incident point vortex, $\epsilon = 1$: (*a*) far-field acoustic pressure as a function of retarded time; (*b*) angular fibre displacement as a function of non-dimensional time. Initial vortex placement is $Z_0 = -10 + 3\mathrm{i}$. (Online version in colour.)

(b) Aeroelastic vortex–fibre interactions

The modelling framework is now demonstrated for the aeroelastic case of a incident vortex with initial position $Z = -10 + 3\mathrm{i}$ and a mean background flow with strength $\epsilon = 1$, recalling that ϵ is defined by (2.8) as the ratio of the mean flow speed to the characteristic vortex speed. The elastic equilibrium fibre position is set to $\theta_0 = 0.5$, and the aeroelastic parameters representative of an owl down fibre in air are $\Omega = 0.761$, $c_\mathrm{d} = 1.85 \times 10^{-3}$ and $\mu = 0.130$, as detailed in appendix C. Three vortex–fibre interaction scenarios are explored and compared to one another with respect to the predicted vortex paths and acoustic signatures: (i) a rigid fibre; (ii) a flexible fibre that is initially still at the elastic equilibrium position $\theta_0 = 0.5$ and (iii) a flexible fibre that is initially still but is displaced away from elastic equilibrium at $\theta = 0.6$. In the latter case, the fibre oscillates under free vibration before the aeroelastic coupling to the incident vortex affects its dynamical response. Lastly, some qualitative changes in the acoustic emission and fibre dynamics are investigated for various initial vertical locations of the incoming vortex.

Figure 7*a* presents and compares the far-field acoustic prediction for each vortex–fibre scenario. For the aeroelastic parameters considered here, the case of the fibre initially at the equilibrium position yields an acoustic signature that is indistinguishable from the rigid fibre case. The corresponding low-amplitude angular displacement history shown in figure 7*b* corroborates the minor influence of the fibre motion on the noise generation. However, the impact of aeroelastic vortex–fibre coupling on the acoustic emission is more substantial for the case when the fibre is initially displaced away from static equilibrium. In this case, figure 7*b* demonstrates that the frequency of fibre oscillation is modulated higher when under the influence of the incident vortex. The acoustic signal for this case is suggestive of a superposition of the rigid-fibre noise signature with higher-frequency oscillatory content that is due to the fibre oscillations. This high-frequency content is modulated in the same manner as the time history of θ in figure 7*b* and indicates that the changes in the acoustic signature arise primarily from the fibre oscillatory motions; the fact that the vortex paths of these three cases are virtually coincident lends support to this claim. The additional noise component due to fibre motions increases the peak acoustic pressure value in the aeroelastic case.

Figure 8 plots the paths of the incident vortex given the initial position $Z_0 = -6 + Y_0\mathrm{i}$ with $\epsilon = 1$. The coincident paths for the aeroelastic cases mentioned above fall on the line for

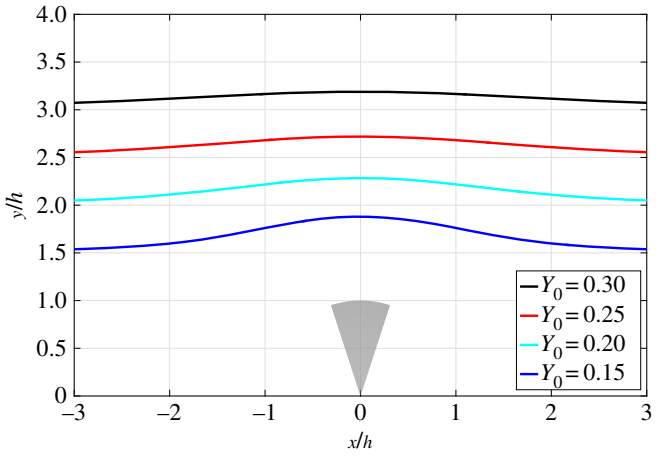

Figure 8. Trajectories of an incident point vortex passing a flexible fibre of frequency that rotates under aeroelastic influence. Initial vortex placement $Z_0 = -6 + Y_0\mathrm{i}$, $\epsilon = 1$. The grey sector indicates the region in which the fibre oscillates during the strongest encounter when $Y_0 = 0.15$. (Online version in colour.)

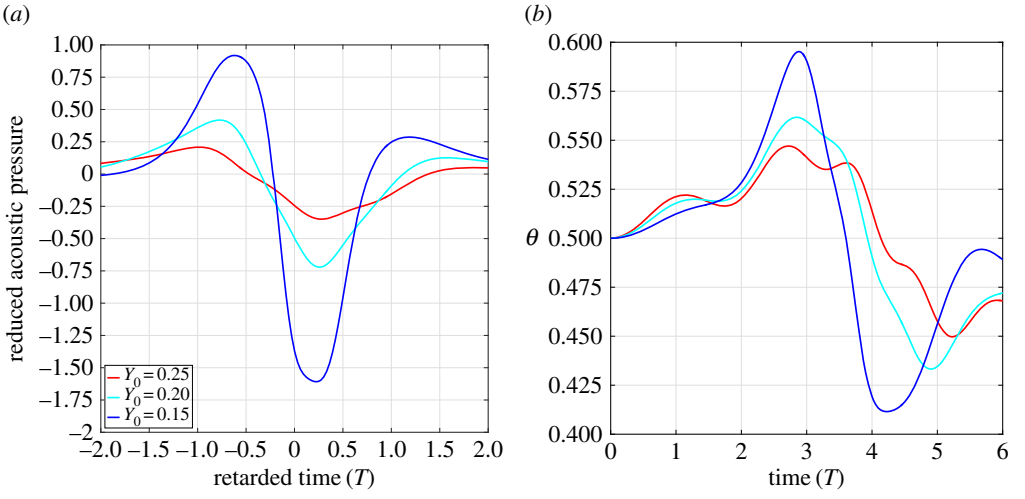

Figure 9. Dynamic and acoustic responses of a flexible fibre immersed in a uniform flow that is aeroelastically coupled to an incident point vortex as a function of initial vertical position, $\epsilon = 1$: (*a*) far-field acoustic pressure as a function of retarded time; (*b*) angular fibre displacement as a function of non-dimensional time. Initial vortex placement $Z_0 = -6 + Y_0\mathrm{i}$. (Online version in colour.)

$Y_0 = 0.3$, and the influence of the fibre on the upward motion of the incoming vortex increases with decreasing Y_0. Figure 9 shows the corresponding acoustic signals and displacement histories of the fibre, where the ringing of the fibre at its natural frequency at large Y_0 in figure 9*b* becomes suppressed by stronger vortex–fibre interactions for lower initial vortex placements. This change in fibre motion is accompanied in figure 9*a* by stronger acoustic peaks and changes in the acoustic response waveform as Y_0 decreases. However, it remains unclear from these results alone whether the fibre could instead be aeroelastically tuned for vortex sound suppression due to the weak differences between the cases of the rigid and flexible cases of the fibre initially at the equilibrium position.

4. Conclusion

A mathematical framework is developed to model the nonlinear trajectory of a vortex under self-induced motion moving past an oscillating two-dimensional barrier in a wedge. The wedge formulation enables subsequent analysis of roughness and trailing-edge noise problems with an elastic extension. In the limit of the wedge forming a half-plane, the problem of vortex-noise generation from a single two-dimensional barrier (fibre) is carried out, corresponding to the limit of a sparse distribution of owl down barbules (pennula) on the upper wing surface. The prescribed harmonic motion of the fibre leads generally to an increase in the extrema in the acoustic signature as the fibre oscillation frequency and background mean flow velocity are increased. However, the phase between the vortex path and fibre motion can lead to noise reductions by altering the vortex trajectory to increase the minimum distance between the vortex and fibre, and by reducing the relative speed between the vortex and fibre when in close proximity. For the range of parameters considered, the acoustic emission of the vortex interaction with the solid surface dominates the acoustic radiation attributed solely to the fibre motion.

Aeroelastic parameters representative of an isolated owl down fibre in air furnish a preliminary assessment of vortex–fibre coupling effects on the motion of the incident vortex and the resulting acoustic emission. For the set of parameters considered, the acoustic signatures of a rigid or flexible fibre that is at static equilibrium at the initial instant are virtually identical. If the flexible fibre is initially displaced away from equilibrium, the aeroelastic coupling between the incident vortex and fibre modulates the fibre dynamic response, and the acoustic response appears as a superposition of the rigid fibre case with higher-frequency sound that depends upon the fibre motion. Preliminary exploration of aeroelastic effects on the noise production and fibre dynamics indicate that at close proximity the coupled vortex–fibre interaction dominates the free vibration dynamics of the fibre, which is accompanied by a change in the waveform of the acoustic response. Additional work is needed to determine whether or not the hydroelastically coupled motion of the vortex and fibre would lead to an increase or decrease in the acoustic level, and in case of the latter event, the parametric ranges where a noise reduction is possible. Further research into the vortex sound generated by flexible trailing edges is also desired and may be pursued using the present dynamic conformal mapping framework.

Data accessibility. This article has no additional data.

Competing interests. I declare I have no competing interests.

Funding. This work was supported in part by the Office of Naval Research under award N00014-14-1-0242, the Air Force Office of Scientific Research under awards FA9550-15-1-0148 and FA9550-19-1-0095, and the National Science Foundation under awards 1805692 and 1846852.

Acknowledgements. The author thanks Mr P. J. Baddoo for bringing to his attention the dynamic Schwarz–Christoffel mapping by Lighthill. The insightful comments and suggestions of the anonymous reviewers are gratefully acknowledged. In particular, the author is indebted to an anonymous reviewer for their derivation of the complex potential for the kinematic boundary condition, which has been adapted in appendix A. Preliminary versions of this paper were presented as conference papers by the author [29,30].

Appendix A. Complex potential of kinematic boundary condition

The physical requirement that the flow cannot penetrate the (moving) solid boundary produces an additional term that must be included in the total complex velocity of the vortex–fibre system. This kinematic boundary condition may be written in vector form as

$$\mathbf{u} \cdot \mathbf{n} = \mathbf{U} \cdot \mathbf{n} \quad \text{on } \partial D, \tag{A 1}$$

where $\mathbf{u}$ is the fluid velocity, $\mathbf{n}$ is the normal vector into the fluid on the fluid–solid boundary ∂D, and $\mathbf{U}$ is the velocity of the boundary, which is identically zero except on the fibre surface. Boundary condition (A 1) may be reexpressed in complex form by noting that along ∂D, which

is parametrized here by the arc length s, the tangent vector $\mathbf{t}$ is $\mathrm{d}z/\mathrm{d}s$ and the normal vector $\mathbf{n}$ becomes $\mathrm{i}\mathrm{d}z/\mathrm{d}s$. The complexification of the velocity vectors to $u(s)$ and $U(s)$ converts (A 1) into

$$\mathrm{Re}\left[\bar{u}(s)\times \mathrm{i}\frac{\mathrm{d}z}{\mathrm{d}s}\right]=\mathrm{Re}\left[\bar{U}(s)\times \mathrm{i}\frac{\mathrm{d}z}{\mathrm{d}s}\right]. \tag{A 2}$$

One can clearly write $\bar{u}=\mathrm{d}w/\mathrm{d}z$ by introducing complex velocity potential $w(z)$ that is associated with the kinematic boundary condition, which enables the bracketed term on the left-hand side to be expressed compactly as $\mathrm{i}\mathrm{d}w/\mathrm{d}s$ via the chain rule. The angular velocity of the fibre is $\mathrm{i}\pi z\mathrm{d}\theta/\mathrm{d}t$ for points z along the fibre, which permits (A 2) to be expressed as

$$\mathrm{Re}\left[\mathrm{i}\frac{\mathrm{d}w}{\mathrm{d}s}\right]=\mathrm{Re}\left[\pi\frac{\mathrm{d}\theta}{\mathrm{d}t}\bar{z}\frac{\mathrm{d}z}{\mathrm{d}s}\right]. \tag{A 3}$$

The identity $(\mathrm{d}/\mathrm{d}s)|z|^2=2\mathrm{Re}[\bar{z}(\mathrm{d}z/\mathrm{d}s)]$ enables (A 3) to be directly integrated in s, where the integration constant may be set to zero without loss of generality. Therefore, the complex velocity associated with kinematic boundary condition satisfies

$$\mathrm{Re}\left[\mathrm{i}w\right]=\frac{\pi}{2}\frac{\mathrm{d}\theta}{\mathrm{d}t}|z|^2\quad\text{on }\partial D. \tag{A 4}$$

Now suppose a kinematic boundary condition mapped to the ζ-plane (cf. figure 2) where $W(\zeta)\equiv w(z(\zeta))$. The goal is to determine an analytic function $\widetilde{W}(\zeta)=\mathrm{i}W(\zeta)$ such that the real part of $\widetilde{W}$ equals the right-hand side of (A 4). Straightforward application of the Cauchy integral formula for Dirichlet boundary value problems on a half plane yields

$$\widetilde{W}(\zeta)=\frac{1}{2\pi\mathrm{i}}\int_{-\infty}^{\infty}\frac{\frac{\pi}{2}(\mathrm{d}\theta/\mathrm{d}t)|z_{\mathrm{f}}(\chi)|^2}{\chi-\zeta}\,\mathrm{d}\chi, \tag{A 5}$$

where $z_{\mathrm{f}}(\xi)$ denotes the values z on the fibre surface in the mapped ζ-plane. Therefore, the complex velocity potential of interest which satisfies the kinematic boundary condition simplifies to

$$W(\zeta)=-\frac{h^2}{4}\frac{\mathrm{d}\theta}{\mathrm{d}t}\int_{-1}^{1}\frac{|Z_{\mathrm{f}}(\chi)|^2}{\chi-\zeta}\,\mathrm{d}\chi. \tag{A 6}$$

The integral in (A 6) has been put into non-dimensional form using $z_{\mathrm{f}}=hZ_{\mathrm{f}}$, where

$$|Z_{\mathrm{f}}(\xi)|=\frac{(1+\xi)^{1-\theta}(1-\xi)^{1-\alpha+\theta}}{g(\alpha,\theta)}. \tag{A 7}$$

Note that the dependence of (A 7) on θ makes $|Z_{\mathrm{f}}|$ an implicit function of time.

Appendix B. Unsteady moment integrals

Unsteady contributions from the linearized Bernoulli equation to the total hydrodynamic moment (2.11) depend on the integrals

$$M_1=\int_{-1}^{1}I_{M_1}(\xi,\alpha,\theta)\,\kappa(\xi,\alpha,\theta)\,\mathrm{d}\xi, \tag{B 1}$$

$$M_2=\int_{-1}^{1}I_{M_2}(\xi,\alpha,\theta)\,\kappa(\xi,\alpha,\theta)\,\mathrm{d}\xi \tag{B 2}$$

and

$$M_3=\left(\frac{\partial\xi_0}{\partial s^*}+\frac{1}{\eta_0}\frac{\partial\eta_0}{\partial s^*}\right)\int_{-1}^{1}\frac{4\eta_0}{(\xi-\xi_0)^2+\eta_0^2}\kappa(\xi,\alpha,\theta)\,\mathrm{d}\xi, \tag{B 3}$$

where

$$I_{M_1}(\xi,\alpha,\theta)=\frac{1}{4}\fint_{-1}^{1}\frac{|Z_f(\chi,\alpha,\theta)|^2}{\chi-\xi}\,\mathrm{d}\chi, \tag{B 4}$$

$$I_{M_2}(\xi,\alpha,\theta)=-\frac{1}{2}\fint_{-1}^{1}\frac{m(\chi,\alpha,\theta)}{\chi-\xi}\,\mathrm{d}\chi, \tag{B 5}$$

$$\kappa(\xi,\alpha,\theta)=(1+\xi)^{1-2\theta}(\xi-b)(1-\xi)^{1-2\alpha+2\theta} \tag{B 6}$$

and

$$m(\chi,\alpha,\theta)=\left[\ln\frac{1+\chi}{1-\chi}+\ln\frac{1-\alpha+\theta}{1-\theta}\right]\frac{(1+\chi)^{2(1-\theta)}(1-\chi)^{2(1-\alpha+\theta)}}{g^2(\alpha,\theta)}. \tag{B 7}$$

Cauchy principal values must be taken where indicated by the dashed integral, and it is implicitly understood that $\theta=\theta(T)$ such that (B 1)–(B 3) are functions of time. Note that the vortex position Z maps to point $\zeta=\xi_0(T)+\eta_0(T)$ in the ζ-plane. The partial derivatives $\partial\xi_0/\partial s^*$ and $\partial\eta_0/\partial s^*$ are readily found from differentiating (2.1) along a streamline with non-dimensional arc length $s^*=s/h$ passing through the instantaneous vortex location and by taking the real or imaginary part.

Appendix C. Estimation of parameters based on owl pennula

Approximate order-of-magnitude estimates of the fibre dynamics parameters are determined in this appendix based on physical characteristics of flexible pennula on the upper surface of owl wings (cf. figure 1). In the sparsely distributed limit, an isolated pennulum is modelled as a cantilevered elastic cylindrical rod of diameter d. Assuming a linear load profile along the length of the fibre, the equivalent torsional spring stiffness at the root of a rigid fibre that yields the same fibre tip deflection of an elastic rod with the same load profile is $k_\theta=(5\pi/22)Ed^4/h$, where E is the elastic modulus. The mass moment of inertia per unit depth into the page for the fibre of thickness d is $I_0\approx(\sqrt{\pi}/6)\rho_f h^3 d$, where ρ_f is the fibre volumetric density.

The natural frequency of the rigid fibre mounted to a torsional spring is $\omega_\theta^2=k_\theta/I_\theta$. The rotational total mass I_θ is the sum of the physical rotational inertia and the effective mass of the fluid surrounding the fibre when oscillating, $(\pi/4)\rho d^2$ [31]. The square of the natural frequency can then be written as

$$\omega_\theta^2=\frac{15}{22}\frac{E}{\rho_f d^2}\left(1+\frac{\rho}{\rho_f}\right)^{-1}\left(\frac{d}{h}\right)^2. \tag{C 1}$$

An approximate Reynolds number can be formed based on $\omega_\theta h$, which in air at standard conditions is $R_{\omega_\theta}\approx 1.6$; this value is consistent with diameter-based Reynolds number estimates of $R=O(1)$ for owl pennula [32]. The damping coefficient c_θ is crudely modelled here on the basis of a viscous drag restoring moment, $c_\theta\approx(1/6)\rho\omega_\theta h^3 d C_D$. The drag coefficient in air for $R=1.6$ is taken to be $C_D\approx 4.8$ using the drag model of Tomotika & Aoi [33, fig. 6].

The material properties of the feather keratin that forms the owl pennula are similar to polypropylene, which has handbook values of $\rho_f\approx 900\,\mathrm{kg\,m^{-3}}$ and $E\approx 2\,\mathrm{GPa}$ (cf. [11]). The pennula have representative dimensions $d\approx 6\,\mu\mathrm{m}$ and $h\approx 1\,\mathrm{mm}$ [34]. The vortex speed parameter is assumed to be approximately at the convective speed of eddies near a wall, $S\approx 0.7U$ [35], where $U=8\,\mathrm{m\,s^{-1}}$ is a representative owl flight speed [17,36].

The dimensionless parameters in (2.10) can now be estimated from the above information: $\Omega=\omega_\theta h/S\approx 0.761$, $c_\mathrm{d}=c_\theta/(2I_0\omega_\theta)\approx 1.85\times 10^{-3}$, and $\mu=I_0/(\rho h^4)\approx 0.130$.

References

1. Graham RR. 1934 The silent flight of owls. *J. R. Aeronaut. Soc.* **38**, 837–843. (doi:10.1017/S0368393100109915)
2. Hersh AS, Soderman PT, Hayden RE. 1974 Investigation of acoustic effects of leading-edge serrations on airfoils. *J. Aircr.* **11**, 197–202. (doi:10.2514/3.59219)

3. Mathews JR, Peake N. 2018 An analytically-based method for predicting the noise generated by the interaction between turbulence and a serrated leading edge. *J. Sound Vib.* **422**, 506–525. (doi:10.1016/j.jsv.2018.02.024)
4. Ffowcs Williams JE, Hall LE. 1970 Aerodynamic sound generation by turbulent flow in the vicinity of a scattering half plane. *J. Fluid Mech.* **40**, 657–670. (doi:10.1017/S0022112070000368)
5. Crighton DG, Leppington FG. 1970 Scattering of aerodynamic noise by a semi-infinite compliant plate. *J. Fluid Mech.* **43**, 721–736. (doi:10.1017/S0022112070002690)
6. Crighton DG. 1972 Acoustic edge scattering of elastic surface waves. *J. Sound Vib.* **22**, 25–32. (doi:10.1016/0022-460X(72)90841-3)
7. Cannell PA. 1975 Edge scattering of aerodynamic sound by a lightly loaded elastic half-plane. *Proc. R. Soc. Lond. A* **347**, 213–238. (doi:10.1098/rspa.1975.0206)
8. Cannell PA. 1976 Acoustic edge scattering by a heavily loaded elastic half-plane. *Proc. R. Soc. Lond. A* **350**, 71–89. (doi:10.1098/rspa.1976.0096)
9. Howe MS. 1992 Sound produced by an aerodynamic source adjacent to a partly coated, finite elastic plate. *Proc. R. Soc. Lond. A* **436**, 351–372. (doi:10.1098/rspa.1992.0023)
10. Howe MS. 1993 Structural and acoustic noise produced by turbulent flow over an elastic trailing edge. *Proc. R. Soc. Lond. A* **442**, 533–554. (doi:10.1098/rspa.1993.0120)
11. Jaworski JW, Peake N. 2013 Aerodynamic noise from a poroelastic edge with implications for the silent flight of owls. *J. Fluid Mech.* **723**, 456–479. (doi:10.1017/jfm.2013.139)
12. Cavalieri AVG, Wolf WR, Jaworski JW. 2016 Numerical solution of acoustic scattering by finite perforated elastic plates. *Proc. R. Soc. A* **472**, 20150767. (doi:10.1098/rspa.2015.0767)
13. Ayton LJ. 2016 Acoustic scattering by a finite rigid plate with a poroelastic extension. *J. Fluid Mech.* **791**, 414–438. (doi:10.1017/jfm.2016.59)
14. Lilley GM. 1998 A study of the silent flight of the owl. In *4*th *AIAA/CEAS Aeroacoustics Conf., Toulouse, France*. Paper AIAA-1998-2340. (doi:10.2514/6.1998-2340)
15. Clark IA, Devenport W, Jaworski JW, Daly C, Peake N, Glegg S. 2014 The noise generating and suppressing characteristics of bio-inspired rough surfaces. In *20*th *AIAA/CEAS Aeroacoustics Conf., Atlanta, GA, USA*. Paper AIAA-2014-2911. (doi:10.2514/6.2014-2911)
16. Clark IA, Alexander WN, Devenport W, Glegg S, Jaworski JW, Daly C, Peake N. 2015 Bio-inspired trailing edge noise control. In *21*st *AIAA/CEAS Aeroacoustics Conf., Dallas, TX, USA*. Paper AIAA-2015-2365. (doi:10.2514/6.2015-2365)
17. Jaworski JW, Peake N. 2020 Aeroacoustics of silent owl flight. *Annu. Rev. Fluids Mech.* **52**, 395–420. (doi:10.1146/annurev-fluid-010518-040436)
18. Kasoev SG. 1976 Sound radiation from a linear vortex over a plane with a projecting edge. *Sov. Phys. Acoust.* **22**, 71–72.
19. Abou-Hussein H, DeBenedictis A, Harrison N, Kim M, Rodrigues MA, Zagadou F, Howe MS. 2002 Vortex-surface interaction noise: a compendium of worked examples. *J. Sound Vib.* **252**, 883–918. (doi:10.1006/jsvi.2001.3833)
20. Howe MS. 2003 *Theory of vortex sound*. Cambridge, UK: Cambridge University Press.
21. Lighthill MJ. 1973 On the Weis-Fogh mechanism of lift generation. *J. Fluid Mech.* **60**, 1–17. (doi:10.1017/S0022112073000017)
22. Milne-Thomson LM. 1968 *Theoretical hydrodynamics*, 5th edn. New York, NY: Dover.
23. Batchelor GK. 1967 *An introduction to fluid dynamics*. Cambridge, UK: Cambridge University Press.
24. Howe MS. 1997 Influence of separation on sound generated by vortex-step interaction. *J. Fluids Struct.* **11**, 857–872. (doi:10.1006/jfls.1997.0113)
25. Michelin S, Llewellyn Smith SG. 2009 An unsteady point vortex method for coupled fluid–solid problems. *Theor. Comput. Fluid Dyn.* **23**, 127–153. (doi:10.1007/s00162-009-0096-7)
26. Manela A, Huang L. 2013 Point vortex model for prediction of sound generated by a wing with flap interacting with a passing vortex. *J. Acoust. Soc. Am.* **133**, 1934–1944. (doi:10.1121/1.4792246)
27. Darakananda D, Eldredge JD. 2019 A versatile taxonomy of low-dimensional vortex models for unsteady aerodynamics. *J. Fluid Mech.* **858**, 917–948. (doi:10.1017/jfm.2018.792)
28. Eldredge JD, Jones AR. 2019 Leading-edge vortices: mechanics and modeling. *Annu. Rev. Fluid Mech.* **51**, 75–104. (doi:10.1146/annurev-fluid-010518-040334)
29. Jaworski JW. 2016 Vortex sound generation from flexible fibers. In *22*nd *AIAA/CEAS Aeroacoustics Conf., Lyon, France*. Paper AIAA-2016-2752. (doi:10.2514/6.2016-2752)

30. Jaworski JW. 2018 Hydroelastic motions of flexible fibers. In *2018 AIAA/CEAS Aeroacoustics Conf., Atlanta, GA, USA*. Paper AIAA-2018-3786. (doi:10.2514/6.2018-3786)
31. Dong RG. 1978 Effective mass and damping of submerged structures. Technical Report UCRL-52342, Lawrence Livermore Laboratory, Berkeley, CA: University of California.
32. Clark IA, Daly CA, Devenport W, Alexander WN, Peake N, Jaworski JW, Glegg S. 2016 Bio-inspired canopies for the reduction of roughness noise. *J. Sound Vib.* **385**, 33–54. (doi:10.1016/j.jsv.2016.08.027)
33. Tomotika S, Aoi T. 1950 The steady flow of viscous fluid past a sphere and circular cylinder at small Reynolds numbers. *Q. J. Mech. Appl. Mech.* **3**, 141–161. (doi:10.1093/qjmam/3.2.141)
34. Klän S, Burgmann S, Bachmann T, Klaas M, Wagner H, Schröder W. 2012 Surface structure and dimensional effects on the aerodynamics of an owl-based wing model. *Eur. J. Mech. B Fluids* **33**, 58–73. (doi:10.1016/j.euromechflu.2011.12.006)
35. Chase DM. 1980 Modeling the wavevector-frequency spectrum of turbulent boundary layer wall pressure. *J. Sound Vib.* **70**, 29–67. (doi:10.1016/0022-460X(80)90553-2)
36. Kroeger RA, Gruschka HD, Helvey TC. 1972 Low speed aerodynamics for ultra-quiet flight. Technical Report AFFDL-TR-71-75, Air Force Flight Dynamics Laboratory, Wright-Patterson AFB.